





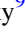




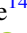
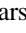




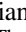







A Multiwavelength Investigation of Spiral Structures in $z > 1$ Galaxies with JWST

Boris S. Kalita^{1,2,3,25} , Si-Yue Yu¹ , John D. Silverman^{1,4,5} , Emanuele Daddi⁶ , Luis C. Ho^{2,7} , Andreas L. Faist⁸ ,
Miroslava Dessauges-Zavadsky⁹ , Annagrazia Puglisi^{10,26} , Simon Birrer¹¹ , Daichi Kashino¹² , Xuheng Ding¹³ ,
Jeyhan S. Kartaltepe¹⁴ , Zhaoxuan Liu^{1,3,4} , Darshan Kakkad¹⁵ , Francesco Valentino^{16,17} , Olivier Ilbert¹⁸ ,
Georgios Magdis^{16,19,20} , Arianna S. Long²¹ , Shuowen Jin^{16,22,27} , Anton M. Koekemoer²³ , and Richard Massey²⁴ 

¹ Kavli IPMU (WPI), UTIAS, The University of Tokyo, Kashiwa, Chiba 277-8583, Japan; boris.kalita@ipmu.jp, kalita.boris.sindhu@gmail.com

² Kavli Institute for Astronomy and Astrophysics, Peking University, Beijing 100871, People's Republic of China

³ Center for Data-Driven Discovery, Kavli IPMU (WPI), UTIAS, The University of Tokyo, Kashiwa, Chiba 277-8583, Japan

⁴ Department of Astronomy, School of Science, The University of Tokyo, 7-3-1 Hongo, Bunkyo, Tokyo 113-0033, Japan

⁵ Center for Astrophysical Sciences, Department of Physics & Astronomy, Johns Hopkins University, Baltimore, MD 21218, USA

⁶ CEA, Irfu, DAp, AIM, Université Paris-Saclay, Université de Paris, CNRS, F-91191 Gif-sur-Yvette, France

⁷ Department of Astronomy, School of Physics, Peking University, Beijing 100871, People's Republic of China

⁸ Caltech/IPAC, MS 314-6, 1200 E. California Blvd. Pasadena, CA 91125, USA

⁹ Department of Astronomy, University of Geneva, 51 Chemin Pegasi, 1290 Versoix, Switzerland

¹⁰ School of Physics and Astronomy, University of Southampton, Highfield SO17 1BJ, UK

¹¹ Department of Physics and Astronomy, Stony Brook University, Stony Brook, NY 11794, USA

¹² National Astronomical Observatory of Japan, 2-21-1 Osawa, Mitaka, Tokyo 181-8588, Japan

¹³ School of Physics and Technology, Wuhan University, Wuhan 430072, People's Republic of China

¹⁴ Laboratory for Multiwavelength Astrophysics, School of Physics and Astronomy, Rochester Institute of Technology, 84 Lomb Memorial Drive, Rochester, NY 14623, USA

¹⁵ Centre for Astrophysics Research, University of Hertfordshire, College Lane, Hatfield AL10 9AB, UK

¹⁶ Cosmic Dawn Center (DAWN), Denmark

¹⁷ Niels Bohr Institute, University of Copenhagen, Jagtvej 128, DK-2200 Copenhagen N, Denmark

¹⁸ Aix Marseille Univ, CNRS, CNES, LAM, Marseille, France

¹⁹ DTU-Space, Technical University of Denmark, Elektrovej 327, 2800, Kgs. Lyngby, Denmark

²⁰ Niels Bohr Institute, University of Copenhagen, Jagtvej 128, DK-2200, Copenhagen, Denmark

²¹ Department of Astronomy, The University of Washington, Seattle, WA 98195, USA

²² DTU-Space, Technical University of Denmark, Elektrovej 327, 2800 Kgs. Lyngby, Denmark

²³ Space Telescope Science Institute, 3700 San Martin Dr., Baltimore, MD 21218, USA

²⁴ Department of Physics, Centre for Extragalactic Astronomy, Durham University, South Road, Durham DH1 3LE, UK

Received 2024 November 20; revised 2024 December 27; accepted 2025 January 2; published 2025 January 29

Abstract

Recent JWST observations have revealed the prevalence of spiral structures at $z > 1$. Unlike in the local Universe, the origin and the consequence of spirals at this epoch remain unexplored. We use public JWST/NIRCam data from the COSMOS-Web survey to map spiral structures in eight massive ($>10^{10.5} M_{\odot}$) star-forming galaxies at $z_{\text{spec}} \sim 1.5$. We present a method for systematically quantifying spiral arms at $z > 1$, enabling direct measurements of flux distributions. Using rest-frame near-IR images, we construct morphological models accurately tracing spiral arms. We detect offsets (~ 0.2 – 0.8 kpc) between the rest-frame optical and near-IR flux distributions across most arms. Drawing parallels to the local Universe, we conclude that these offsets reflect the presence of density waves. For 9 out of 18 arms, the offsets indicate spiral shocks triggered by density waves. In all, 5 arms have offsets in the opposite direction and are likely associated with tidal interactions. For the remaining cases with no detected offsets, we suggest that stochastic “clumpy” star formation is the primary driver of their formation. In conclusion, we find a multifaceted nature of spiral arms at $z > 1$, similar to that in the local Universe.

Unified Astronomy Thesaurus concepts: [Spiral galaxies \(1560\)](#); [Galaxy evolution \(594\)](#)

1. Introduction

Over 60% of galaxies in the local Universe feature some level of spiral structure (P. B. Nair & R. G. Abraham 2010; K. W. Willett et al. 2013; R. J. Buta et al. 2015). Nevertheless, the origin and consequences of spiral arms have been debated for nearly a century (e.g., E. P. Hubble 1926; J. H. Reynolds 1927; G. de Vaucouleurs 1959; D. M. Elmegreen et al. 1982). Given

the current understanding (see C. Dobbs & J. Baba 2014; F. H. Shu 2016, for a review), the main lines of inquiry can be summarized into two key questions: (I) What are the formation mechanisms and physical characteristics of spiral arms? (II) What is their impact on star formation in their hosts? The answer to either question is far from straightforward. This Letter focuses on the first question, aimed at the $z > 1$ Universe, with the second to be explored in a follow-up work.

Decades of observations and simulations have established a few key modes of spiral arm formation: the quasi-stationary density-wave theory, producing long-lived “grand design” spirals (F. H. Shu 1970; A. Toomre 1977; F. H. Shu 2016); transient, recurrent spiral arms (J. A. Sellwood & R. G. Carlberg 1984; R. Bottema 2003; M. S. Fujii et al. 2011; J. Baba et al. 2013); local instability amplifications leading to “flocculent” spirals (M. W. Mueller & W. D. Arnett 1976;

²⁵ Kavli Astrophysics Fellow.

²⁶ Anniversary Fellow.

²⁷ Marie Curie Fellow.



H. Gerola & P. E. Seiden 1978; D. M. Elmegreen & B. G. Elmegreen 1987); and perturbations from tidal interactions (A. Toomre & J. Toomre 1972; H. Salo & E. Laurikainen 2000; C. L. Dobbs et al. 2010). Emerging theories, such as manifolds (for bar-driven spirals; e.g., E. Athanassoula et al. 2009) and groove instability (J. A. Sellwood & R. G. Carlberg 2019), also offer new interpretations of spiral arm formation. Notably, these processes are not mutually exclusive and can coexist within a galaxy (D. M. Elmegreen & B. G. Elmegreen 2014; S.-Y. Yu & L. C. Ho 2020).

The quasi-stationary or transient density-wave theory assumes a constant pattern speed that differs from the differentially rotating disk (except at the corotation radius, where both velocities match). Across most of the disk, within the corotation radius, the arms are expected to trail behind the disk. The kinematics of such a system is predicted to manifest as a color gradient across the width of the spiral arms (D. M. Gittins & C. J. Clarke 2004; E. E. Martínez-García et al. 2009). Some studies suggest these trends reflect stellar age gradients (R. A. Gonzalez & J. R. Graham 1996; E. E. Martínez-García & R. A. González-Lópezlira 2013), while others argue that color gradients also arise from attenuation due to dust lanes along spiral arms (S.-Y. Yu & L. C. Ho 2018; E. E. Martínez-García et al. 2023) produced by spiral shocks (R. Lynds 1970; D. M. Gittins & C. J. Clarke 2004). However, this evidence comes from only a few cases. Tidal interactions have also been suggested to produce density waves that trail the disk (A. J. Kalnajs 1973; J. Binney & S. Tremaine 2008; S. H. Oh et al. 2008), although strong perturbations could result in leading waves (M. Thomasson et al. 1989; R. Buta et al. 1992; R. J. Buta et al. 2003).

Meanwhile, some formation modes produce spiral arms that are expected to corotate with the disk. Stochastic star formation can lead to overdense areas of stars, which are then sheared by the disk's differential rotation to form spirals (M. W. Mueller & W. D. Arnett 1976; H. Gerola & P. E. Seiden 1978; J. P. Sleath & P. Alexander 1995; H. Nomura & H. Kamaya 2001). These local instability-driven flocculent spirals are not grand design spirals but rather a patchwork of short, irregular arms. Tidal interactions can also create material arms that shear into corotating spirals (A. Toomre 1969; S. E. Meidt & E. Schinnerer 2013). Thus, observational evidence of rotational velocity offsets has the potential to reveal the mechanisms behind spiral arm formation. However, the observational results discussed so far are limited to the local Universe.

Spiral arms in the $z > 1$ regime have been relatively unexplored. The redshift range of $z = 1-3$ (cosmic noon) is, however, a critical phase of our Universe. In addition to marking the peak of the star formation rate (SFR) density (P. Madau & M. Dickinson 2014), significant morphological evolution of galaxies is expected (P. Lang et al. 2014; S. Toft et al. 2014). While discussions have largely focused on the buildup of central mass concentrations (e.g., D. Elbaz et al. 2018; C. Gómez-Guijarro et al. 2018; A. Puglisi et al. 2021; Q.-H. Tan et al. 2024a, 2024b) and disk dynamics (T. Contini et al. 2016; J. P. Stott et al. 2016; C. M. Harrison et al. 2017; L. Posti et al. 2018; A. Marasco et al. 2019; S. Gillman et al. 2020), the evolution of key disk features like bars and spirals has received less attention (D. M. Elmegreen & B. G. Elmegreen 2014; B. Margalef-Bentabol et al. 2022; E. E. Martínez-García et al. 2023; S.-Y. Yu et al. 2023; Y. Guo et al. 2024). Characterization

of spirals at $z > 1$ have mainly relied on visual classifications, which provide valuable insight into the variety of such features.

With the advent of high-resolution JWST data revealing an abundance of spirals (e.g., C. Jacobs et al. 2023; V. Kuhn et al. 2024; Z. Liu et al. 2024; J. McKinney et al. 2024; M. Polletta et al. 2024), it is crucial to begin more detailed investigations of spirals during cosmic noon. This work initiates such an effort. Using JWST/NIRCam data for detailed modeling and flux distribution analysis, we aim to detect color gradients indicative of velocity offsets between spiral arms and the host disk. We construct the first method for a systematic quantification of spiral arms at $z > 1$ and make direct flux distribution measurements across rest-frame optical and near-IR wavelengths.

In this Letter, we introduce our sample in Section 2, followed by the analysis and results (Sections 3 and 4, respectively). We conclude with a discussion (Section 5) and summary (Section 6). Throughout, we adopt a concordance Λ CDM cosmology, characterized by $\Omega_m = 0.3$, $\Omega_\Lambda = 0.7$, and $H_0 = 70 \text{ km s}^{-1} \text{ Mpc}^{-1}$. Magnitudes and colors are on the AB scale. All images are oriented such that north is up and east is left.

2. Sample and Data

We use eight galaxies (Figure 1, top panel) from the ($H\alpha$ -detected) FMOS-COSMOS sample (D. Kashino et al. 2013; J. D. Silverman et al. 2015; D. Kashino et al. 2019), selected from 57 star-forming main-sequence galaxies within ~ 0.3 dex of the relation in J. S. Speagle et al. (2014; FMOS-COSMOS-ALMA sample). This sample has been presented in B. S. Kalita et al. (2025) and will be further discussed in upcoming works. These galaxies are spectroscopically confirmed at $1.4 \leq z \leq 1.7$ with stellar masses of $10^{10.5-11.4} M_\odot$ (determined earlier in D. Kashino et al. 2019). As they reside in the COSMOS field (N. Scoville et al. 2007), 48 have multiband (F115W, F150W, F277W, and F444W) JWST/NIRCam coverage from the COSMOS-Web survey (C. M. Casey et al. 2023). After visually inspecting the images, we find 18 of these galaxies clearly display spiral arms. Most of the rest also feature varying degrees of substructures, but they do not resemble spirals. Attempts at quantifying the visual classification will be addressed in upcoming works, since it requires a general estimate of the spiral strength across the full sample. Nevertheless, our “spiral fraction” of $\sim 40\%$ is much higher than the $\lesssim 10\%$ expected at $z \sim 1.5$, found through visual inspections (B. Margalef-Bentabol et al. 2022). We attribute this higher value to the likely bias introduced by the SFR-based selection of the sample. Of the 18 galaxies, 8 are found to be sufficiently uniform and bright (in near-IR) for our analysis, although 2 show signs of interaction with a companion (IDs 449617 and 662400). ID 545623 also has a possible companion but features highly ordered spiral arms.

To map the spiral features in the rest-frame near-IR (tracing stellar mass distribution) and optical (representing unattenuated star formation), we use the F444W and F150W filters from the COSMOS-Web JWST/NIRCam data set. The point-spread functions (PSFs) for each filter are created using the software PSFEX (E. Bertin 2011) on the full COSMOS-Web mosaic. Since dust likely plays a major role in determining flux distribution, we choose F444W over F277W to limit attenuation effects. F150W is preferred over F115W due to the deeper data (5σ AB magnitude depths of 27.4 and 27.1, respectively) and better-sampled PSFs, as the image pixel scale ($0''.03$) in

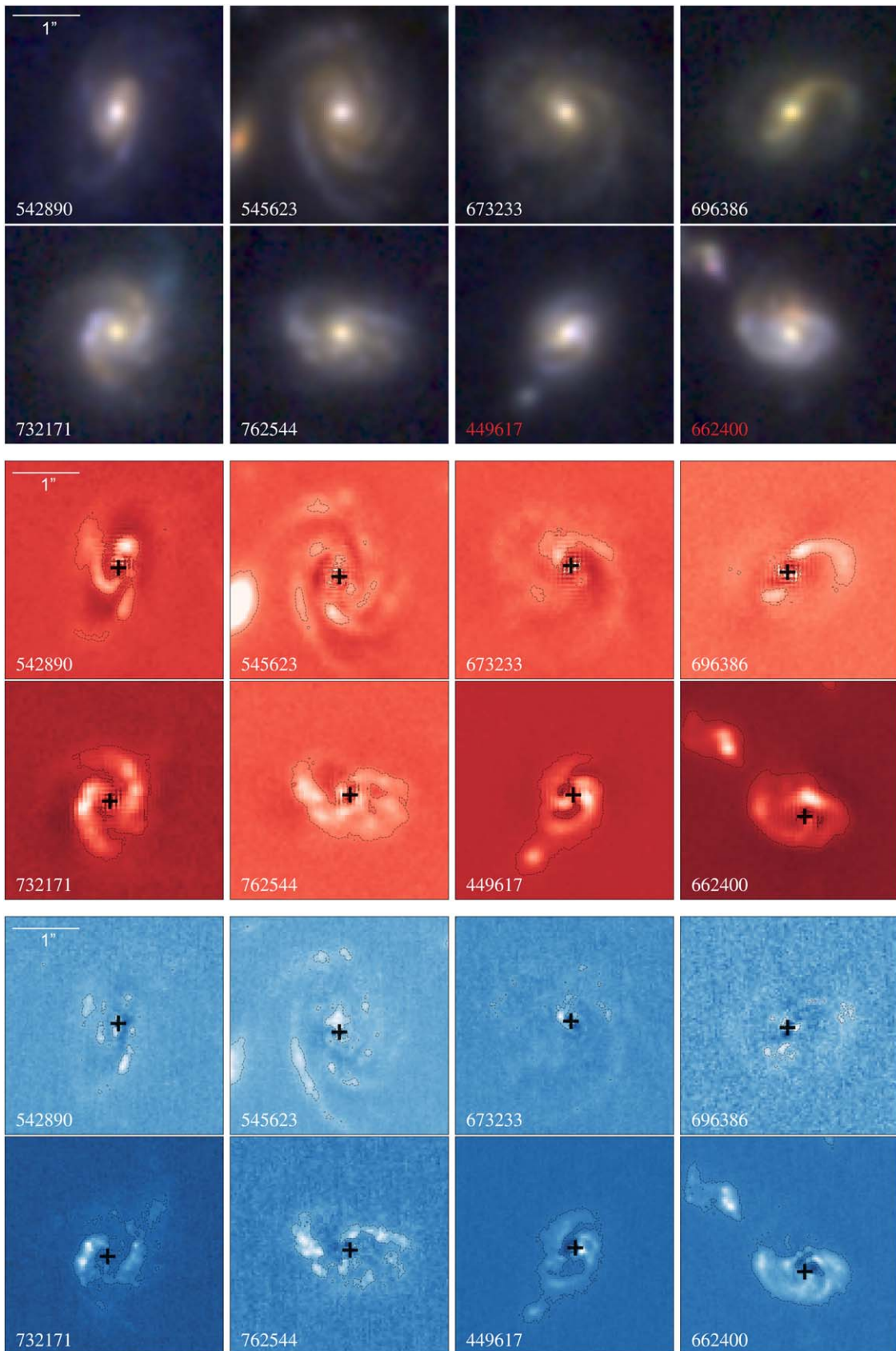


Figure 1. Image compilation of the sample: (top panels) the RGB images (F150W, F277W, F444W) of the 8 galaxies used in this work are 100×100 pixels or $3'' \times 3''$. The COSMOS2015 (C. Laigle et al. 2016) IDs are provided for each galaxy, with the final two in red denoting the possible presence of an interacting companion. All are within a redshift range of $1.43 \leq z \leq 1.74$ and have stellar masses of $10^{10.5-11.4} M_{\odot}$. The corresponding F444W (middle panels, with 5σ contours) and F150W (PSF-matched to F444W, bottom panels, with lower 3σ contours to account for the lower image depth) residual images after subtraction of a bulge and disk model highlight the presence of spiral arms.

F115W is similar to its PSF FWHM ($0''.04$).²⁸ Finally, the F150W image is PSF-matched to the F444W data using a Gaussian kernel.

3. Analysis

3.1. Spirals in the Near-IR Residuals

In this work, we aim to effectively model and quantify the spiral structures in the disk. The first step is to detect disk substructures, which is found to be most efficient by subtracting the underlying disk (along with the bulge; B. S. Kalita et al. 2025). Since the stellar distribution is best traced by the F444W rest-near-IR data, we model the corresponding images of our galaxy sample using Sérsic models. The fitting is performed with the Python-based package GALIGHT²⁹ (X. Ding et al. 2020), which implements the forward-modeling tool LENSTRONOMY³⁰ (S. Birrer & A. Amara 2018; S. Birrer et al. 2021). This approach provides access to the full posterior distribution of each fitted parameter and is optimized using the Particle Swarm Optimizer (PSO; J. Kennedy & R. Eberhart 1995).

We compare the results of a single Sérsic model (without a fixed index) and a composite bulge+disk model (with Sérsic indices $n=2$ and 1 for the bulge and disk, respectively).³¹ Based on the assessment of negative peaks in the residual images, reduced χ^2 , and the Bayesian information criterion (BIC; which combines model complexity with χ^2), we conclude that the bulge+disk model consistently outperforms the single Sérsic model, with the $-\Delta\text{BIC}$ found to be $>10^3$. In the final residual near-IR images, after bulge+disk subtraction, the underlying spiral structures are clearly visible (Figure 1, middle panel). We do not refer to any specific flux or σ threshold here since we already limit this study to galaxies where our spiral arm modeling method is successful. As mentioned in Section 2, a generalized determination of the flux values at which spiral arms can be successfully studied will be addressed in upcoming works. Finally, we create a residual optical (F150W) image by subtracting a bulge+disk model with shape parameters fixed to those from F444W and only fitting for flux. The resulting images are provided in Figure 1 (bottom panel) and will be used in Section 3.3.

3.2. Determining Spiral Arm Locations

Our goal is to measure the flux distribution over the spiral arms. To do so, we first need to locate the arms. This is typically achieved in the local Universe by performing discrete Fourier decomposition in polar coordinates and then using the power spectrum to determine spiral arm characteristics (see S.-Y. Yu et al. 2018 for a discussion). However, we find that such methods do not enable characterization of spirals at $z > 1$, due to the combined effects of weaker spiral arm strengths, irregularities, and additional substructures. Additionally, we find the arms become significantly more discontinuous in rest-frame optical wavelengths, further complicating characterization.

The challenge of locating the arms directly from Fourier space information can be overcome by using shape priors in the image plane that are spiral models. Hence, we devise a modified method for locating spiral arms in our galaxy sample at $z \sim 1.5$. We first deproject the residual images onto a circular geometry using the axis ratio from the rest-frame near-IR disk fit (Section 3.1). This is done by rotating the image (to align the disk's major axis with the x -axis) and decomposing it in the Cartesian coordinate system into shapelets using LENSTRONOMY. The image grid is then adjusted so the final axis ratio of the disk becomes 1. Since each galaxy in our sample already has an axis ratio >0.7 , the change introduced is minimal.

The deprojected images (Figure 2, first column) are then passed through a polar-shapelet transform (using LENSTRONOMY), where all azimuthal components except $m=2, 3$, and 4 are filtered out. Higher-order modes are sensitive to noise (S. Kendall et al. 2011; S.-Y. Yu et al. 2021), as well as “galaxy clumps” expected at these redshifts (e.g., R. Genzel et al. 2011; Y. Guo et al. 2015; A. Claeysens et al. 2023; Z. Sattari et al. 2023; B. S. Kalita et al. 2024). This step isolates structures that peak 2, 3, or 4 times per full rotation about the galaxy center (determined from the rest-frame near-IR bulge+disk model). This method successfully extracts the spiral patterns, as can be seen in Figure 2 (second column). It is also noteworthy that the deprojection is essential for this step to work properly as any residual circular component of the disk could be picked up as an $m=2$ component due to projection effects.

The final part of the analysis aims to model the spiral structures. To do so, we add back the now symmetric disk (deprojected version of the GALIGHT disk model with $n=1$) that was previously subtracted. This is essential since the spiral pattern on its own cannot be fit due to the presence of negative residuals. The final disk+spiral image is modeled using GALFIT (C. Y. Peng et al. 2010), resulting in the final model of the spiral structures.³² Once fit, we artificially amplify the spiral arms by increasing the amplitude of the Fourier components of the GALFIT model (Figure 2, third column). These models are used to generate segmentation maps (Figure 2, fourth column), excluding the bulge (up to the effective radius in the rest-frame near-IR). The spiral arm paths (Figure 3) are then traced on the segmentation maps using the SKELETONIZE function from the SKIMAGE³³ Python package.

For the final part of the analysis, we use GALFIT because it includes the option to fit spiral components, a feature missing in GALIGHT. However, for the initial bulge+disk fitting, we prefer GALIGHT as its PSO optimization outperforms the χ^2 -minimization approach of GALFIT, especially in the presence of strong substructures, which are common in our sample. Due to the same reason, we are also unable to fit a bulge+disk+spiral model in GALFIT.

3.3. Mapping Flux across the Arms

From here onward, we only rely on the arm paths (Figure 3) determined in the previous section and no longer use the GALFIT models. We measure the flux along the spiral arms (radially outward) in steps of 2 pixels up to a radial distance of

²⁸ An undersampled PSF can lead to systematic biases in spatial measurements.

²⁹ <https://github.com/dartoon/galight>

³⁰ <https://github.com/lenstronomy/lenstronomy>

³¹ We ensure that using a classical bulge with $n=4$ does not change our results. However, we use the value for a pseudobulge (D. B. Fisher & N. Drory 2008) since the central region is star forming throughout our sample.

³² We use a Sérsic model for the disk with spiral subcomponents with varying amplitudes that are fit to the disk+spiral image.

³³ <https://scikit-image.org/>

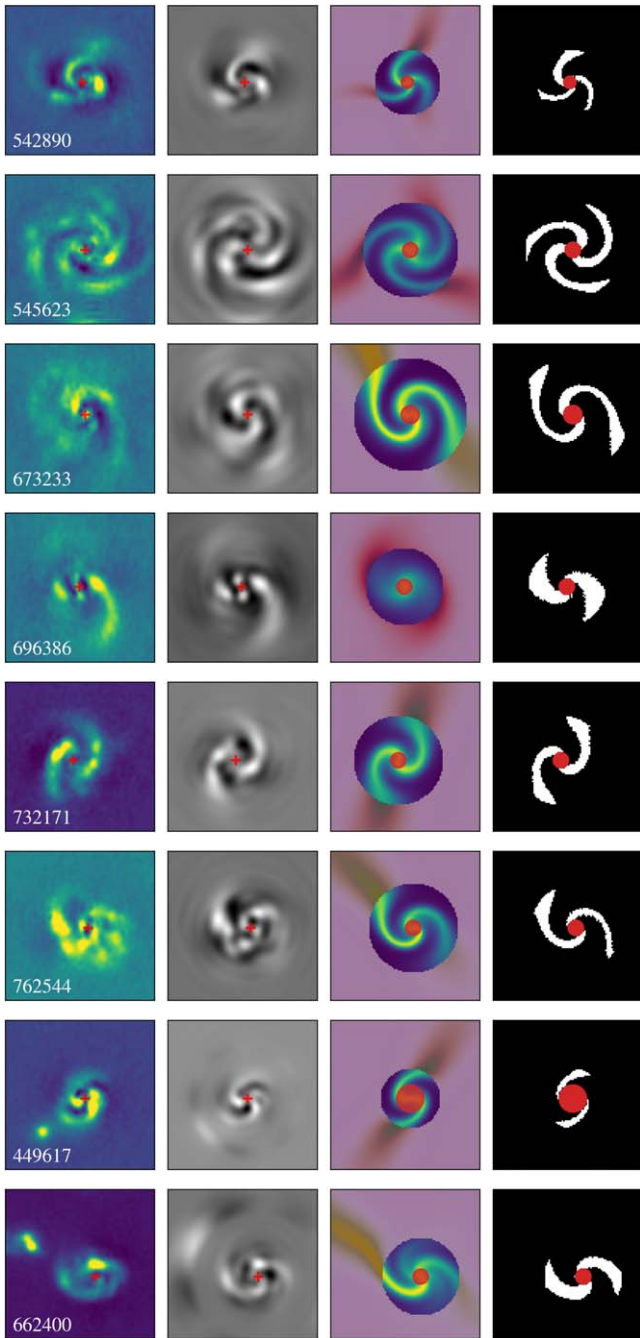


Figure 2. Locating the spiral arms: the deprojected residual F444W images (first column), the same image with only the $m = 2-4$ components (second column), the GALFIT best-fit model for the disk+spiral components with the spiral arms amplified (as discussed in Section 3.2; third column), and the segmentation regions created out of the model (fourth column) for each galaxy in our sample. The segmentation maps will be used to trace the location of each spiral arm. The red circles in the middle and right panels denote the bulge (effective radius), which has been excluded. The outer circle in the third panel shows the radial limit of the analysis, which is twice the disk effective radius.

$2\times$ the effective radius of the disk in the rest-frame near-IR. The per-pixel flux distribution is mapped at every step over a mask of 15 pixels in length (~ 4 kpc at $z = 1.5$) and 3 pixels in width ($\sim 1.3\times$ the FWHM of the F444W PSF). At each iteration, the radial direction of the arm is determined, and the mask length is kept perpendicular to it. Flux measurements are made for the deprojected residual images in both the rest-frame optical (F150W) and near-IR (F444W), mapping the variation

along the mask's length while collapsing (averaging) over the width. Results for two of the galaxies are shown in Figure 4 (left and right). Also shown are two example masks, with the longer edge of each across the spiral arm being their lengths.

We locate the peak of flux distribution across the spiral arms by fitting a skewed Gaussian model over the length of each mask. The positional error is given by the 1σ uncertainty of the fit. We check the centroid as well as the peak of the flux distributions and find them to be in agreement with the model peak within the respective uncertainties. To estimate the systematic uncertainty of our procedure, we add an artificial point source to a source-free region of the data and perform the same deprojection procedure as in Section 3.2. We then reverse the process, concluding that any systematic offset introduced in the first half would remain at the end of the full procedure. We estimate an uncertainty of ~ 0.5 pixel width (~ 0.13 kpc at $z = 1.5$). The other source of uncertainty, due to intrinsic noise fluctuations, is already accounted for by this process. We exclude the polar-shapelet transform from this error estimate as it is used only to determine mask position and orientation.

4. Results

Within the sample of eight galaxies, we detect and model 18 spiral arms (Figure 2). For each arm, we measure the flux variation at each iteration step. In all, 15/18 arms show a peak F444W flux $\geq 5\sigma$ over 60%–100% of their lengths (contours shown in Figure 1, middle panel). For the remaining 3, the fraction of length being detected drops to $\sim 10\%$ –30%. In contrast, the “well-detected” 15/18 arms have a peak F150W flux $\geq 5\sigma$ over $\sim 10\%$ –80% of their lengths. However, considering the F150W image is 0.5 mag shallower than F444W, a more appropriate threshold is $\sim 3\sigma$, where arms are detected over 20%–90% of their lengths (contours shown in Figure 1, bottom panel). The final three arms, which had lower F444W detections, are not detected in the F150W data. Given that the flux per unit frequency (F_ν) should remain almost constant over the rest-frame wavelength range covered by F150W and F444W at $z = 1.5$ for a constant star formation model without dust attenuation, there is clear reddening in the arms, likely caused by dust or stellar age. Since spiral arms are predominantly star forming, attenuation likely plays a major role. The three arms that were weakly detected in F444W were likely pushed below our F150W detection thresholds due to attenuation.

We also find clear spatial offsets between the flux distributions in F444W and F150W based on their flux peaks (Figure 4). Additionally, we assign a direction to the spiral arms based on the expected propagation for density waves (Figure 4). A positive offset indicates that the near-IR flux lags behind the optical flux, while a negative offset shows the reverse. We observe that the offset is not constant along the arms but shows clear radial variations (Figure 5). Averaging over the length of the spiral arms, the offsets for the 15/18 arms with both F444W and F150W detections are mostly within -0.2 kpc to 0.4 kpc, with one exception at -0.4 kpc. Given our spatial uncertainty of 0.13 kpc, this suggests a marginal bias toward positive values.

However, given the radial variation, the average is not a robust tracer of the offsets. We rather determine the maximum offset for each arm by finding the location where the following

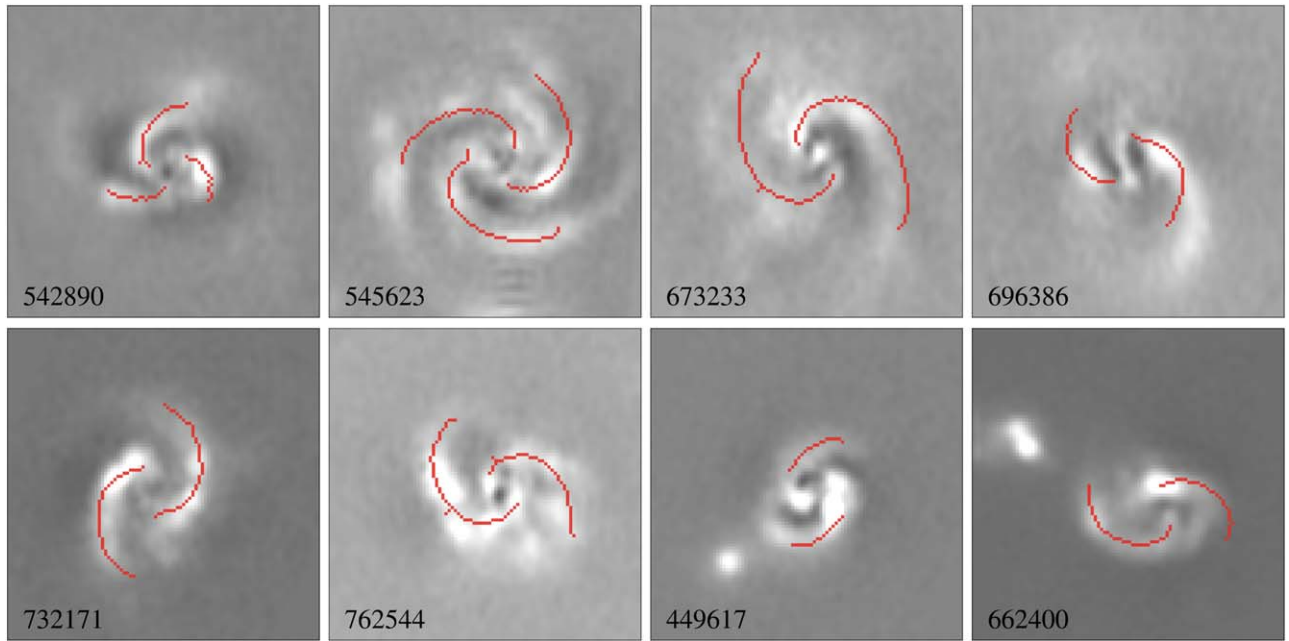


Figure 3. The model-based spiral skeletons overlaid on the deprojected residual F444W images of the galaxies in our sample.

parameter (F) is maximized:

$$F = \alpha |\text{offset}| + (1 - \alpha) \text{significance}. \quad (1)$$

Here, the “offset” is the difference between the F150W and F444W flux peaks. The “significance” refers to the ratio of the offset and the corresponding error. This allows us to determine the maximum offset not just based on the absolute value but also the significance. We choose $\alpha = 0.5$ to allow an equal contribution from both these parameters. The radial locations of the maximum offsets for arms in two of the galaxies in our sample (the same as in Figure 4) are provided in Figure 5. In all, 10/15 detected arms show positive offsets, with 9 of these showing offsets greater than our systematic uncertainty (~ 0.13 kpc; Section 3.3) ranging from 0.2 to 0.8 kpc (Figure 6). Meanwhile, 5/15 arms show negative values from -0.2 to -0.8 kpc, with 3 of these arms found in two galaxies (IDs 449617 and 662400) showing clear signs of interaction.

5. Discussions

In this section, we shall be proposing that the observed offset between the flux peaks in rest-frame near-IR and optical wavelengths indicates density-wave propagation, either quasi-static or transient. For long-lived quasi-static spirals, the wave-like arms have fixed angular velocities. Thus, below the corotation radius, the arms propagate slower than the differentially rotating disk (trailing arms). However, in the case of transient waves, deviations from a fixed angular velocity are expected. Nevertheless, we generally still expect trailing arms (C. Dobbs & J. Baba 2014).

As gas in the disk falls into the potential of these trailing arms, it can be accelerated to the speed of sound, creating shocks. The initial “spiral shock” would therefore lag behind the arm (W. W. Roberts 1969). The compression of the gas clouds causes part of the gas to lose angular momentum and flow inward (Y. Kim & W.-T. Kim 2014), while some of it forms new stars and moves through the density wave

(W. W. Roberts 1969; D. M. Gittins & C. J. Clarke 2004). The majority of the dust produced in this process, tracing the location of the shock, resides on the leading side of the rest-frame near-IR arm (S.-Y. Yu & L. C. Ho 2018). As a result, the optical flux from the newly formed young stars is attenuated, while the young stars that have moved past the slowly propagating arm experience less attenuation. This combination produces an optical wavelength flux concentration in front of the arm.

The positive offsets we observe in half of the spiral arms in our sample match these expectations (Figures 4 and 6), assuming the arms are predominantly below the corotation radius. Furthermore, in the case of quasi-static density waves, the positive offset should gradually decrease with increasing radius as the corotation radius is approached. The lowering of the positive offset in galaxy ID 732171 at the highest radial distances for both of its spiral arms (Figure 5, left panel) could be interpreted as a sign of such a gradient. However, proper quantification of this effect will require larger statistics and kinematic information.

Within the density-wave scenario, the offset magnitude will be influenced by the time lag between gas compression and star formation, the dust distribution, and the velocity offset between the arm and the disk. Disentangling these factors will be crucial to understanding the dynamics of the spiral arm relative to the underlying disk. Deeper submillimeter images tracing dust emission and spectroscopic data providing the velocities of different disk components will be necessary. Nevertheless, the observed red-to-blue gradient aligns well with studies on density-wave propagation at low redshifts ($0 \lesssim z \lesssim 1$; S.-Y. Yu & L. C. Ho 2018; E. E. Martínez-García et al. 2023). These studies also predict a secondary blue-to-red gradient from aging stars moving away from the arms, which future studies should investigate.

Meanwhile, five arms show a clear negative offset (e.g., Figure 4, right panel). It is worth noting that none of the respective host galaxies simultaneously feature arms with positive offsets. Explaining this through density waves requires

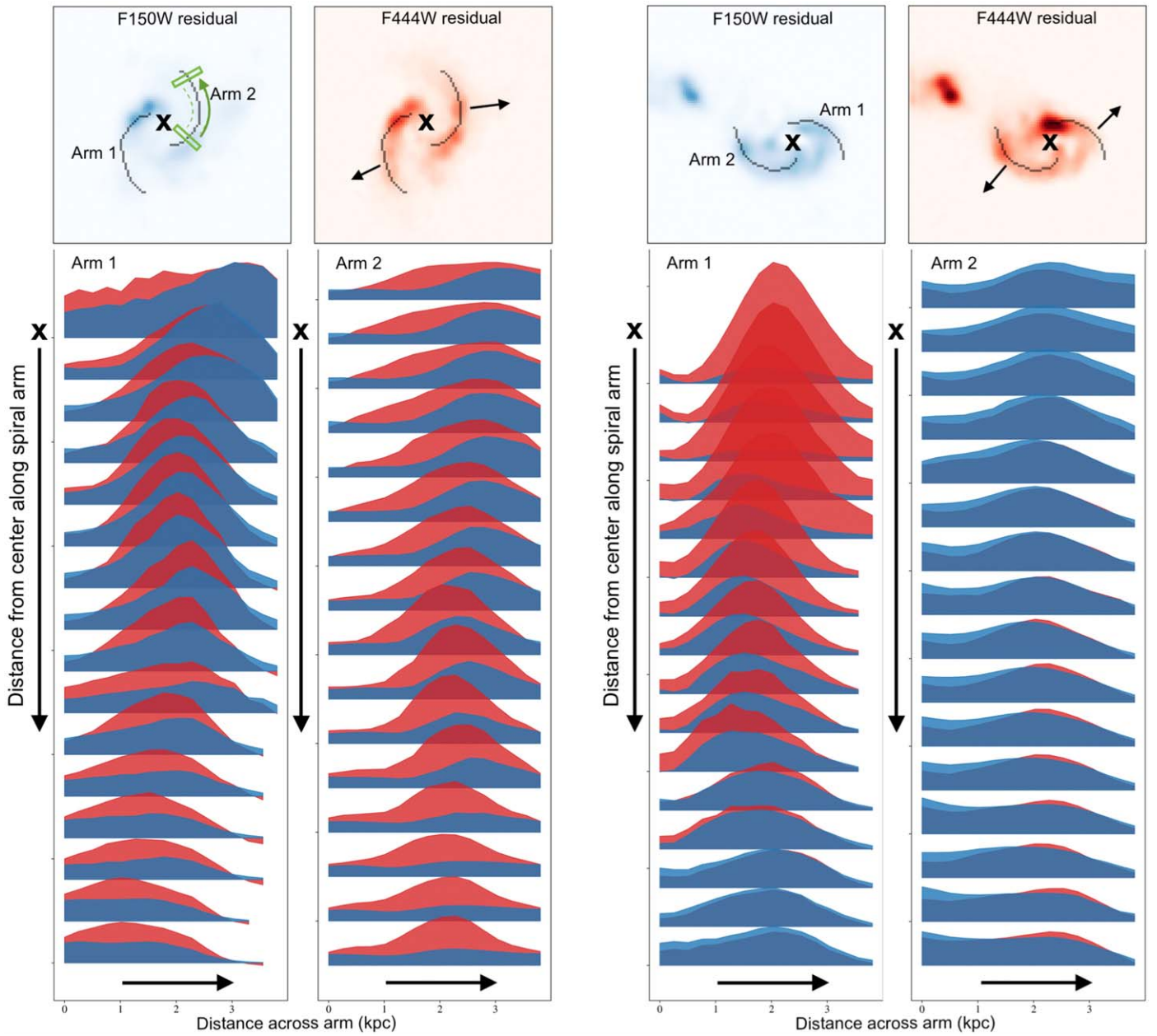


Figure 4. (Left) Positive color offsets in ID 732171: (top panels) residual F150W and F444W images after bulge and disk subtraction, with spiral arm paths overlotted and expected propagation direction indicated by arrows. The first image on the top left also shows examples of the masks perpendicular to the arm used for flux measurements, with the longer edge being the length of the mask. (Lower panels) Flux distribution (all distributions at same flux scale) across each arm and along the length of the masks, with F150W in blue and F444W in red, for the first 16 pixels (~ 4 kpc) along the arms starting from the center of the galaxy (marked with “x”). The distributions show clear positive offsets, with blue generally preceding red. The same arm propagation direction defines the x-axis (in kiloparsecs, calculated for $z = 1.5$) ordering. The y-axis corresponds to the measurement bins along the arms, representing radial distance from the galaxy center in kiloparsecs. The first 16 iterations, with 2 pixel steps, are shown for each arm. (Right) Negative color offsets in ID 662400: The same information, but for a case showing negative offsets. The blue F150W flux distribution generally trails behind the red F444W distribution.

invoking motion beyond the corotation radius while simultaneously observing positive offsets at lower radii, which we do not observe. Instead, some local cases show waves from interactions causing arms to move faster than the disk medium (R. Buta et al. 1992; R. J. Buta et al. 2003). We may be observing a similar effect here, especially since minor mergers increase with redshift (J. M. Lotz et al. 2011), making them common at $z \sim 1.5$. In this scenario, the spiral arms are density waves accelerated by the external potential of a companion. Three of the five arms with a negative offset appear in the two interacting galaxies in our sample, supporting this conclusion.

Finally, three arms are not detected in rest-frame optical (F150W) while being marginally detected in rest-frame near-IR (F444W). These cases likely involve formation mechanisms without velocity offsets, such as interaction-driven material arms or stochastic star formation. The latter is hypothesized to produce weak flocculent spirals (H. Gerola & P. E. Seiden 1978; B. Jungwiert & J. Palous 1994; J. P. Sleath & P. Alexander 1995), which would be difficult to model. Stochastic star formation is also important because galaxies at $z > 1$ are highly clumpy (e.g., B. G. Elmegreen et al. 2008; N. M. Förster Schreiber et al. 2011; R. Genzel et al. 2011;

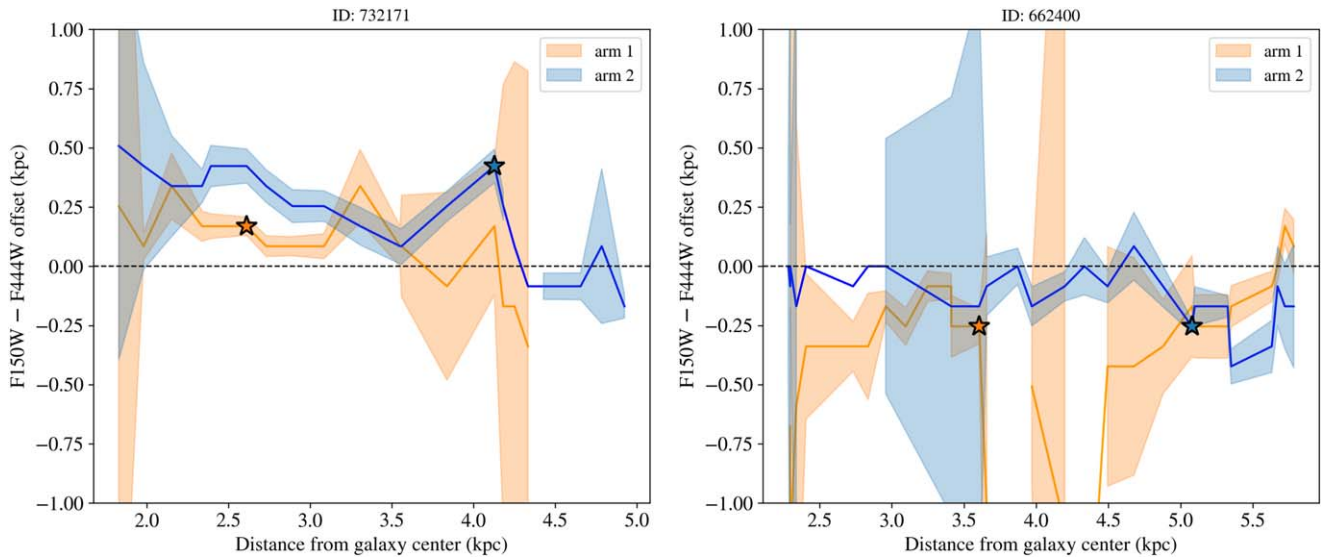


Figure 5. Radial distribution of offsets: the radial variation of the offset between the peaks of the F150W and F444W flux distributions across the spiral arms for the galaxies shown in Figure 4—IDs 732171 (left) and 662400 (right). The corresponding shaded regions indicate the 1σ uncertainties. The stars show the data point taken as the maximum offset value, determined using the maximum absolute value and the corresponding uncertainty.

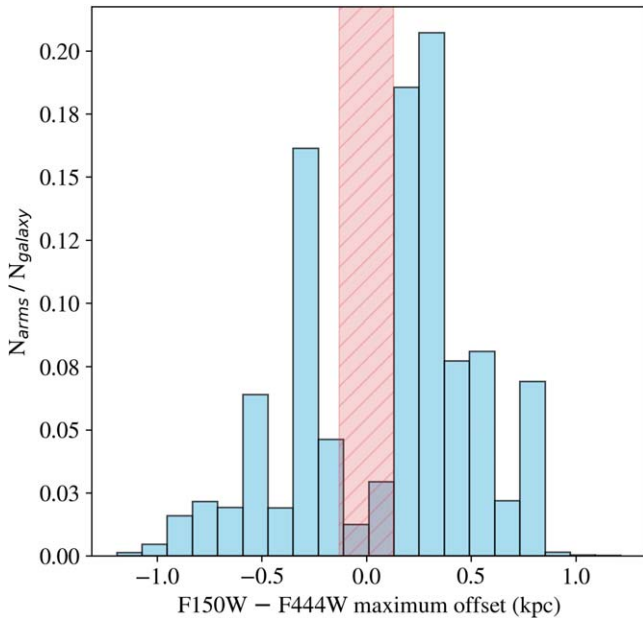


Figure 6. Maximum offset distribution: the normalized number distribution of the maximum offset between the F150W and F444W flux distributions across the spiral arms in our sample. For our sample, $N_{\text{galaxy}} = 8$. The x -axis is shown in kiloparsecs (for $z = 1.5$). We create this histogram by randomly sampling values (1000 times) within the 1σ error margins for each maximum offset measurement. The total uncertainty of our method is estimated to be ~ 0.13 kpc, so values within 0 ± 0.13 kpc (region in red) are considered to indicate no offset.

A. Claeysens et al. 2023; Z. Sattari et al. 2023; A. L. Faisst et al. 2024; B. S. Kalita et al. 2024), driven by high gas fractions (E. Daddi et al. 2010; L. J. Tacconi et al. 2010; J. E. Geach et al. 2011; W. Rujopakarn et al. 2023), leading to large fractions of star formation (up to $\sim 25\%$) concentrated in kiloparsec-scale complexes. The resulting massive clumps can be sheared by the rotating disk, leading to spiral structures (D. M. Elmegreen & B. G. Elmegreen 2014; R. Genzel et al. 2023). We also expect to be underestimating its impact in our study, having excluded galaxies with faint, patchy arms—key

traits of flocculent spirals. Hence, spiral arms in such galaxies would probably appear in the region between the positive and negative peaks in Figure 6. Furthermore, feedback from star formation may also erase key signatures of density-wave spirals (R. Shetty & E. C. Ostriker 2008; C. L. Dobbs et al. 2011), complicating assessments of formation mechanisms.

6. Summary

We use JWST/NIRCam data for eight massive star-forming galaxies (stellar mass = $10^{10.5-11.4} M_{\odot}$) at $z_{\text{spec}} \sim 1.5$ to characterize their spiral arms in detail. Using Cartesian and polar-shapelet transforms, we isolate the spiral structures in rest-frame near-IR and construct models. These models chart the radial paths along the spirals, allowing us to iteratively measure the flux distribution along these paths and across the width of the arms in PSF-matched rest-frame optical (F150W NIRCam filter) and near-IR (F444W NIRCam filter) residual images.

We find that all 18 spiral arms in our sample are detected at $\geq 5\sigma$ significance in the stellar mass–tracing near-IR wavelength. However, 3/18 are entirely absent in rest-frame optical, and in the remaining arms, the detected length fraction significantly decreases compared to the near-IR, likely due to attenuation by dust known to exist in spiral arms. Half of the arms show robust levels of red-to-blue color gradient along the expected direction of arm propagation. Drawing parallels to the local Universe, we interpret this gradient as an indicator of dust from shocks caused by density-wave-driven spiral propagation, where the arms are slower than the disk’s circular velocity. Conversely, 5 arms display a blue-to-red gradient, likely due to tidal interaction perturbations. Arms without any gradient are probably driven by interactions or stochastic star formation. We also predict that spirals formed through stochastic star formation may be underrepresented in our study due to their patchy nature, making them challenging to model.

In conclusion, this study provides a quantitative characterization of spiral structures in the $z > 1$ Universe, made possible by JWST. We highlight the complex, multifaceted nature of spiral arms and emphasize the need for further studies to

understand galaxy morphological evolution during this critical epoch.

Acknowledgments

We thank the referee for the valuable comments. B.S.K. and J.D.S. are supported by the World Premier International Research Center Initiative (WPI), MEXT, Japan. J.D.S. is supported by JSPS KAKENHI (JP22H01262). This work was also supported by JSPS Core-to-Core Program (grant No.: JPJSCCA20210003). O.I. acknowledges the funding of the French Agence Nationale de la Recherche for the project iMAGE (grant ANR-22-CE31-0007). L.C.H. was supported by the National Science Foundation of China (11991052, 12233001), the National Key R&D Program of China (2022YFF0503401), and the China Manned Space Project (CMS-CSST-2021-A04, CMS-CSST-2021-A06). This work was made possible by utilizing the CANDIDE cluster at the Institut d'Astrophysique de Paris. The cluster was funded through grants from the PNCG, CNES, DIM-ACAV, the Euclid Consortium, and the Danish National Research Foundation Cosmic Dawn Center (DNR140). It is maintained by Stephane Rouberol. The JWST data presented in this Letter were obtained from the Mikulski Archive for Space Telescopes (MAST) at the Space Telescope Science Institute. The specific observations analyzed can be accessed via DOI:10.17909/04ww-nn64. The data set was obtained as part of the COSMOS-Web survey program (ID 1727). We would finally like to thank Pascal Oesch and Mengyuan Xiao for the valuable discussions.

ORCID iDs

Boris S. Kalita  <https://orcid.org/0000-0001-9215-7053>
 Si-Yue Yu  <https://orcid.org/0000-0002-3462-4175>
 John D. Silverman  <https://orcid.org/0000-0002-0000-6977>
 Emanuele Daddi  <https://orcid.org/0000-0002-3331-9590>
 Luis C. Ho  <https://orcid.org/0000-0001-6947-5846>
 Andreas L. Faisst  <https://orcid.org/0000-0002-9382-9832>
 Miroslava Dessauges-Zavadsky  <https://orcid.org/0000-0003-0348-2917>
 Annagrazia Puglisi  <https://orcid.org/0000-0001-9369-1805>
 Simon Birrer  <https://orcid.org/0000-0003-3195-5507>
 Daichi Kashino  <https://orcid.org/0000-0001-9044-1747>
 Xuheng Ding  <https://orcid.org/0000-0002-0786-7307>
 Jeyhan S. Kartaltepe  <https://orcid.org/0000-0001-9187-3605>
 Zhaoxuan Liu  <https://orcid.org/0000-0002-9252-114X>
 Darshan Kakkad  <https://orcid.org/0000-0002-2603-2639>
 Francesco Valentino  <https://orcid.org/0000-0001-6477-4011>
 Olivier Ilbert  <https://orcid.org/0000-0002-7303-4397>
 Georgios Magdis  <https://orcid.org/0000-0002-4872-2294>
 Arianna S. Long  <https://orcid.org/0000-0002-7530-8857>
 Shuowen Jin  <https://orcid.org/0000-0002-8412-7951>
 Anton M. Koekemoer  <https://orcid.org/0000-0002-6610-2048>
 Richard Massey  <https://orcid.org/0000-0002-6085-3780>

References

- Athanassoula, E., Romero-Gómez, M., & Masdemont, J. J. 2009, *MNRAS*, **394**, 67
 Baba, J., Saitoh, T. R., & Wada, K. 2013, *ApJ*, **763**, 46
 Bertin, E. 2011, in ASP Conf. Ser. 442, *Astronomical Data Analysis Software and Systems XX*, ed. I. J. Evans et al. (San Francisco, CA: ASP), 435
 Binney, J., & Tremaine, S. 2008, *Galactic Dynamics: Second Edition* (Princeton, NJ: Princeton Univ. Press)
- Birrer, S., & Amara, A. 2018, *PDU*, **22**, 189
 Birrer, S., Shajib, A., Gilman, D., et al. 2021, *JOSS*, **6**, 3283
 Bottema, R. 2003, *MNRAS*, **344**, 358
 Buta, R., Crocker, D. A., & Byrd, G. G. 1992, *AJ*, **103**, 1526
 Buta, R. J., Byrd, G. G., & Freeman, T. 2003, *AJ*, **125**, 634
 Buta, R. J., Sheth, K., Athanassoula, E., et al. 2015, *ApJS*, **217**, 32
 Casey, C. M., Kartaltepe, J. S., Drakos, N. E., et al. 2023, *ApJ*, **954**, 31
 Claeysens, A., Adamo, A., Richard, J., et al. 2023, *MNRAS*, **520**, 2180
 Contini, T., Epinat, B., Bouché, N., et al. 2016, *A&A*, **591**, A49
 Daddi, E., Bournaud, F., Walter, F., et al. 2010, *ApJ*, **713**, 686
 de Vaucouleurs, G. 1959, *HDP*, **53**, 275
 Ding, X., Silverman, J., Treu, T., et al. 2020, *ApJ*, **888**, 37
 Dobbs, C., & Baba, J. 2014, *PASA*, **31**, e035
 Dobbs, C. L., Burkert, A., & Pringle, J. E. 2011, *MNRAS*, **417**, 1318
 Dobbs, C. L., Theis, C., Pringle, J. E., & Bate, M. R. 2010, *MNRAS*, **403**, 625
 Elbaz, D., Leiton, R., Nagar, N., et al. 2018, *A&A*, **616**, A110
 Elmegreen, B. G., Bournaud, F., & Elmegreen, D. M. 2008, *ApJ*, **688**, 67
 Elmegreen, D. M., & Elmegreen, B. G. 1987, *ApJ*, **314**, 3
 Elmegreen, D. M., & Elmegreen, B. G. 2014, *ApJ*, **781**, 11
 Elmegreen, D. M., Elmegreen, B. G., & Dressler, A. 1982, *MNRAS*, **201**, 1035
 Faist, A. L., Brinch, M., Casey, C. M., et al. 2024, arXiv:2405.09619
 Fisher, D. B., & Drory, N. 2008, *AJ*, **136**, 773
 Förster Schreiber, N. M., Shapley, A. E., Genzel, R., et al. 2011, *ApJ*, **739**, 45
 Fujii, M. S., Baba, J., Saitoh, T. R., et al. 2011, *ApJ*, **730**, 109
 Geach, J. E., Smail, I., Moran, S. M., et al. 2011, *ApJL*, **730**, L19
 Genzel, R., Jolly, J. B., Liu, D., et al. 2023, *ApJ*, **957**, 48
 Genzel, R., Newman, S., Jones, T., et al. 2011, *ApJ*, **733**, 101
 Gerola, H., & Seiden, P. E. 1978, *ApJ*, **223**, 129
 Gillman, S., Tiley, A. L., Swinbank, A. M., et al. 2020, *MNRAS*, **492**, 1492
 Gittins, D. M., & Clarke, C. J. 2004, *MNRAS*, **349**, 909
 Gómez-Guijarro, C., Toft, S., Karim, A., et al. 2018, *ApJ*, **856**, 121
 Gonzalez, R. A., & Graham, J. R. 1996, *ApJ*, **460**, 651
 Guo, Y., Ferguson, H. C., Bell, E. F., et al. 2015, *ApJ*, **800**, 39
 Guo, Y., Jogee, S., Wise, E., et al. 2024, arXiv:2409.06100
 Harrison, C. M., Johnson, H. L., Swinbank, A. M., et al. 2017, *MNRAS*, **467**, 1965
 Hubble, E. P. 1926, *ApJ*, **63**, 236
 Jacobs, C., Glazebrook, K., Calabrò, A., et al. 2023, *ApJL*, **948**, L13
 Jungwiert, B., & Palous, J. 1994, *A&A*, **287**, 55
 Kalita, B. S., Silverman, J. D., Daddi, E., et al. 2024, *ApJ*, **960**, 25
 Kalita, B. S., Suzuki, T. L., Kashino, D., et al. 2025, *MNRAS*, **536**, 3090
 Kalnajs, A. J. 1973, *PASA*, **2**, 174
 Kashino, D., Silverman, J. D., Rodighiero, G., et al. 2013, *ApJL*, **777**, L8
 Kashino, D., Silverman, J. D., Sanders, D., et al. 2019, *ApJS*, **241**, 10
 Kendall, S., Kennicutt, R. C., & Clarke, C. 2011, *MNRAS*, **414**, 538
 Kennedy, J., & Eberhart, R. 1995, in Proc. ICNN'95—Int. Conf. Neural Networks, 4 (New York: IEEE), 1942
 Kim, Y., & Kim, W.-T. 2014, *MNRAS*, **440**, 208
 Kuhn, V., Guo, Y., Martin, A., et al. 2024, *ApJL*, **968**, L15
 Laigle, C., McCracken, H. J., Ilbert, O., et al. 2016, *ApJS*, **224**, 24
 Lang, P., Wuyts, S., Somerville, R. S., et al. 2014, *ApJ*, **788**, 11
 Liu, Z., Silverman, J. D., Daddi, E., et al. 2024, *ApJ*, **968**, 15
 Lotz, J. M., Jonsson, P., Cox, T. J., et al. 2011, *ApJ*, **742**, 103
 Lynds, R. 1970, *ApJL*, **159**, L151
 Madau, P., & Dickinson, M. 2014, *ARA&A*, **52**, 415
 Marasco, A., Fraternali, F., Posti, L., et al. 2019, *A&A*, **621**, L6
 Margalef-Bentabol, B., Conselice, C. J., Haussler, B., et al. 2022, *MNRAS*, **511**, 1502
 Martínez-García, E. E., & González-Lópezlira, R. A. 2013, *ApJ*, **765**, 105
 Martínez-García, E. E., González-Lópezlira, R. A., & Gómez, G. C. 2009, *ApJ*, **707**, 1650
 Martínez-García, E. E., González-Lópezlira, R. A., & Puerari, I. 2023, *MNRAS*, **524**, 18
 McKinney, J., Casey, C. M., Long, A. S., et al. 2024, arXiv:2408.08346
 Meidt, S. E., Schinnerer, E., García-Burillo, S., et al. 2013, *ApJ*, **779**, 45
 Mueller, M. W., & Arnett, W. D. 1976, *ApJ*, **210**, 670
 Nair, P. B., & Abraham, R. G. 2010, *ApJS*, **186**, 427
 Nomura, H., & Kamaya, H. 2001, *AJ*, **121**, 1024
 Oh, S. H., Kim, W.-T., Lee, H. M., & Kim, J. 2008, *ApJ*, **683**, 94
 Peng, C. Y., Ho, L. C., Impey, C. D., & Rix, H.-W. 2010, *AJ*, **139**, 2097
 Polletta, M., Frye, B. L., Garuda, N., et al. 2024, *A&A*, **690**, A285
 Posti, L., Fraternali, F., Di Teodoro, E. M., & Pezzulli, G. 2018, *A&A*, **612**, L6
 Puglisi, A., Daddi, E., Valentino, F., et al. 2021, *MNRAS*, **508**, 5217
 Reynolds, J. H. 1927, *Obs*, **50**, 185
 Roberts, W. W. 1969, *ApJ*, **158**, 123
 Rujopakarn, W., Williams, C. C., Daddi, E., et al. 2023, *ApJL*, **948**, L8
 Salo, H., & Laurikainen, E. 2000, *MNRAS*, **319**, 377

- Sattari, Z., Mobasher, B., Chartab, N., et al. 2023, *ApJ*, 951, 147
- Scoville, N., Aussel, H., Brusa, M., et al. 2007, *ApJS*, 172, 1
- Sellwood, J. A., & Carlberg, R. G. 1984, *ApJ*, 282, 61
- Sellwood, J. A., & Carlberg, R. G. 2019, *MNRAS*, 489, 116
- Shetty, R., & Ostriker, E. C. 2008, *ApJ*, 684, 978
- Shu, F. H. 1970, *ApJ*, 160, 89
- Shu, F. H. 2016, *ARA&A*, 54, 667
- Silverman, J. D., Kashino, D., Sanders, D., et al. 2015, *ApJS*, 220, 12
- Sleath, J. P., & Alexander, P. 1995, *MNRAS*, 275, 507
- Speagle, J. S., Steinhardt, C. L., Capak, P. L., & Silverman, J. D. 2014, *ApJS*, 214, 15
- Stott, J. P., Swinbank, A. M., Johnson, H. L., et al. 2016, *MNRAS*, 457, 1888
- Tacconi, L. J., Genzel, R., Neri, R., et al. 2010, *Natur*, 463, 781
- Tan, Q.-H., Daddi, E., de Souza Magalhães, V., et al. 2024a, *A&A*, 684, A23
- Tan, Q.-H., Daddi, E., Magnelli, B., et al. 2024b, *Natur*, 636, 69
- Thomasson, M., Donner, K. J., Sundelius, B., et al. 1989, *A&A*, 211, 25
- Toft, S., Smolčić, V., Magnelli, B., et al. 2014, *ApJ*, 782, 68
- Toomre, A. 1969, *ApJ*, 158, 899
- Toomre, A. 1977, *ARA&A*, 15, 437
- Toomre, A., & Toomre, J. 1972, *ApJ*, 178, 623
- Willett, K. W., Lintott, C. J., Bamford, S. P., et al. 2013, *MNRAS*, 435, 2835
- Yu, S.-Y., Cheng, C., Pan, Y., Sun, F., & Li, Y. A. 2023, *A&A*, 676, A74
- Yu, S.-Y., & Ho, L. C. 2018, *ApJ*, 869, 29
- Yu, S.-Y., & Ho, L. C. 2020, *ApJ*, 900, 150
- Yu, S.-Y., Ho, L. C., Barth, A. J., & Li, Z.-Y. 2018, *ApJ*, 862, 13
- Yu, S.-Y., Ho, L. C., & Wang, J. 2021, *ApJ*, 917, 88